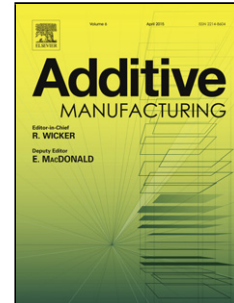


Journal Pre-proof

Investigation of LPBF A800H steel parts using Computed Tomography and Mössbauer spectroscopy

R.R. Gainov (Conceptualization) (Investigation) (Data curation) (Writing - original draft) (Writing - review and editing), D. Faidel (Methodology) (Investigation) (Writing - reviewing and editing), W. Behr (Validation), G. Natour (Supervision), F. Pauly (Investigation) (Validation), H. Willms (Project administration), F.G. Vagizov (Investigation)



PII: S2214-8604(19)31105-4

DOI: <https://doi.org/10.1016/j.addma.2020.101035>

Reference: ADDMA 101035

To appear in: *Additive Manufacturing*

Received Date: 8 August 2019

Revised Date: 11 December 2019

Accepted Date: 1 January 2020

Please cite this article as: Gainov RR, Faidel D, Behr W, Natour G, Pauly F, Willms H, Vagizov FG, Investigation of LPBF A800H steel parts using Computed Tomography and Mössbauer spectroscopy, *Additive Manufacturing* (2020), doi: <https://doi.org/10.1016/j.addma.2020.101035>

This is a PDF file of an article that has undergone enhancements after acceptance, such as the addition of a cover page and metadata, and formatting for readability, but it is not yet the definitive version of record. This version will undergo additional copyediting, typesetting and review before it is published in its final form, but we are providing this version to give early visibility of the article. Please note that, during the production process, errors may be discovered which could affect the content, and all legal disclaimers that apply to the journal pertain.

© 2019 Published by Elsevier.

Investigation of LPBF A800H steel parts using Computed Tomography and Mössbauer spectroscopy

R.R. Gainov^{1,2*}, D. Faidel^{1*}, W. Behr¹, G. Natour¹, F. Pauly¹, H. Willms¹, F.G. Vagizov³

¹ *Central Institute of Engineering, Electronics and Analytics – Engineering and Technology (ZEA-1), Forschungszentrum Jülich GmbH, Wilhelm-Johnen-Str., 52428 Jülich, Germany*

² *Institute of Mineral Resources Engineering (MRE), RWTH Aachen University, Wüllnerstr. 2, 52062 Aachen, Germany*

³ *Kazan Federal University, 420008 Kazan, Kremlevskaya str. 18, Russian Federation*

^{1*} E-mail: gainov@mre.rwth-aachen.de

^{2*} E-mail: d.faidel@fz-juelich.de

ABSTRACT

Laser powder bed fusion (LPBF) was applied in this study to produce a prototype of a miniaturized catalytic burner (CAB), which is a key component of high-temperature polymer electrolyte fuel cells. This prototype was characterized by its complex design with numerous channels, chambers, and thin walls. The test samples and CAB prototype were made of a heat-resistant, anti-corrodible steel called "Alloy 800H" (1.4876), a material that poses problems for welding operations and especially for the LPBF process due to its strong susceptibility to hot cracking and spatters. The effects of LPBF parameter variation on preliminary test samples were investigated by nano-focus Computed Tomography (CT) and Optical microscopy to clarify the internal structure and defects for further LPBF process optimization. Mössbauer spectroscopy points out that LPBF process does not lead to either local phase separation nor oxidation of steel, which is critical factor for use of CAB at high temperatures. The sufficient LPBF parameter sets were used to manufacture the CAB prototype, which was examined by micro-CT and optics as well. The main result of the investigation is a demonstration of the technological feasibility to decrease the number and size of defects in complex LPBF-manufactured Alloy 800H constructions without changes in phase composition at high temperatures.

I. INTRODUCTION

Forschungszentrum Jülich GmbH (FZJ) is one of Europe's largest interdisciplinary research centers with more than 50 institutes and subinstitutes. One of these is the Central Institute of Engineering, Electronics and Analytics – Engineering and Technology (ZEA-1). ZEA-1 designs, develops, and fabricates technical and scientific equipment, instruments, and processes. It is focused on mechanical engineering that is needed for world-class research but is not commercially available. The development of measurement and testing methods is another area of focus. One of the competencies at ZEA-1 is three-dimensional (3D) printing of metallic structures of different sizes and geometries, which are difficult, expensive, or even impossible to manufacture using traditional methods. ZEA-1 also uses selective laser melting (SLM), corresponding to laser powder bed fusion (LPBF) family of 3D-printing techniques, to manufacture scientific equipment for high-vacuum and high-temperature applications. One example of a specific material used in the LPBF process at ZEA-1 is high-temperature-resistant molybdenum powder for manufacturing ultra-high-vacuum parts, as demonstrated by Faidel et al [1].

Generally, LPBF has great potential for use in the aerospace, automotive, medical, and nuclear industries for the production of parts of various sizes, as Bremer et al outlined in their detailed review [2]. The state of the art of LPBF production is reviewed, for example, by Weber [3], who describes the use of LPBF parts in the Orion spacecraft program or in projects focusing on

unmanned aerial vehicles (UAVs) comprising 80% additive manufactured parts. As Klempert states in his discussion of initial approaches to additive manufacturing [4], this technology – similar to LPBF – has prospects for use not only in high-technology areas, but also for implementation in mass production. One of the main challenges in realizing mass production for LPBF is quality management. The advantages of LPBF technology include its ability to facilitate a wide variety of 3D geometries for constructions and its potential to reduce the total manufacturing costs of these constructions.

There are currently considerable efforts being made to improve and control the LPBF process by means of various methods and approaches. One such method is in situ LPBF thermography to detect defects during the manufacturing process, as described in detail by Everton et al [5]. Another such approach for material engineering is complementary techniques of X-ray computed tomography (CT) and neutron tomography (e.g., both methods are considered in [6, 7]), including newly developed Time-of-Flight 3D polarimetric neutron tomography (PNT) [8] and newly designed wide-broad neutron polarizing equipment for this material research field [9]. Up to date CT is an approved universal tool for investigating not only metal parts manufactured using LPBF or electron-beam melting (EBM), but also ceramic and polymer parts produced using processes such as stereolithography (SLA), selective laser sintering (SLS), or fused deposition modeling (FDM). The up-to-date detailed reviews of these processes are provided by Thompson et al [10] and Du Plessis et al [11]. As shown by Shah et al [12], the accuracy and capability of CT, when applied to different additive manufacturing processes, is comparable to reference measurements made by a coordinate measuring machine (CMM). Modeling based on CT-provided information helps to predict and evaluate the mechanisms of pore and crack formation in LPBF-manufactured parts, as shown by Krakhmalev et al [13], for example. Moreover, CT and Archimedes methods show comparable potential for porosity prediction, as demonstrated by Wits et al [10] in their work for the Netherlands Aerospace Center (NLR).

Based on LPBF technology, ZEA-1 recently produced a prototype of a highly integrated (miniaturized) catalytic burner (CAB), as described in detail by Meißner et al [15]. In that paper, the CAB was considered a key component of a new high-temperature polymer electrolyte fuel cell (HT-PEM-FC) system. The paper was published within the scope of a cooperation between ZEA-1 and Institute of Energy and Climate Research – Electrochemical Process Engineering IEK-3, another FZJ subinstitute, which designed the prototype. The present paper is devoted to the initial research conducted into the quality and stability of the CAB prototype produced by ZEA-1.

During this initial research stage, different metal parts for preliminary testing were studied, as well as one fragment of the CAB prototype made from high-temperature "Alloy 800H" (1.4876) steel. The choice of A800H steel was motivated by its unique combination of heat-resistant and anti-corrodible properties, which ensure that the CAB is stable with regard to H₂, CH₄, and CO at high temperatures. On the other hand, as we know from the comprehensive review by Lippold [16], the tendency of this alloy to form "hot cracks" along fusion zone grain boundaries makes it difficult to use even with conventional welding and, as a consequence, its use poses a challenge in the LPBF process. Because of this, the use of Alloy 800H steel in the LPBF process is quite rare and not a trivial manufacturing matter, and requires considerable scientific support.

On this basis, the methodological approach applied in this research involved the combined use of CT and conversion electron ⁵⁷Fe-Mössbauer spectroscopy (CEMS). This is a unique approach for characterizing materials, especially metals, and requires complex, high-precision equipment. Both techniques are non-destructive X-ray methods with similar energy ranges, although they have different focuses. CT was used to clarify the internal structure, heterogeneity, and defects on the macroscale (from a few microns to tens of microns). CEMS (sometimes called nuclear γ -resonance spectroscopy) was used to identify the phase composition on the nano- and microscale after high-temperature manufacturing. The more detailed description of both methods is given in Subsections II.3 and II.4. Optical microscopy in the two-dimensional (2D) regime was applied in a supplementary manner to verify the 3D CT results obtained.

In this paper, we present the results of 3D CT measurements of test samples and CAB parts, including both micro- and nano-focus images at different projections and virtual positions together with Mössbauer spectra, and 2D optical microscopy images of mechanical cuts taken from test samples. In particular, we found that the number and size of defects could be decreased by a combination of different LPBF parameters; we also found that high-temperature LPBF manufacturing does not lead either to phase separation of the steel nor to considerable oxidation. On the basis of the experimental data obtained, we will present and discuss some aspects of the LPBF process and properties of the relevant constructions.

II. MATERIALS AND METHODS

II.1. LPBF technology

Laser powder bed fusion (LPBF) is an additive manufacturing process which allows metal parts to be constructed from different materials and with complex geometries. The process proceeds as follows (Fig. 1): first, a 3D CAD model of the part is sliced into layers with preset thicknesses. Second, the coater in the LPBF machine takes powder from the powder bunker and applies a thin layer to the substrate in the building envelope, according to the preset layer thickness. Third, a laser beam passes through the optics and melts the powder according to the geometry of the slice, and the process then reiterates until the part is fully constructed.

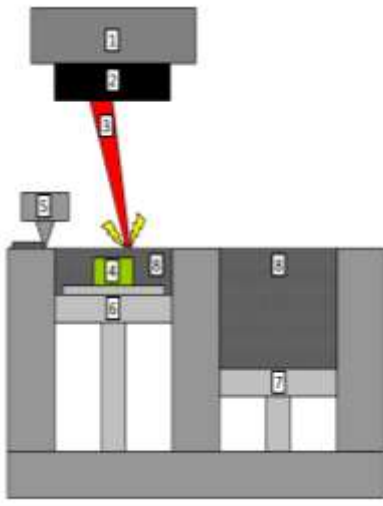


Fig. 1. Concept of the LPBF technology used: 1- laser scanner, 2- laser optics, 3- laser beam, 4- part, 5- coater, 6- building envelope, 7- powder bunker, 8- powder.

The LPBF machine used at ZEA-1 is an upgraded Concept Laser M2 LPBF machine equipped with a new CW fiber laser with 500 W maximum power and a 17 μm fiber core diameter. The laser allows the use of a beam shaper to create not only a Gaussian intensity distribution profile but also donut and top hat profiles, etc. Beam diagnostic equipment is also installed in the machine and the shielding gas atmosphere is reduced to the minimal value of 10 ppm residual oxygen. This machine setup allows parts to be manufactured from both high-temperature materials and highly oxidizing materials due to the high laser intensity of up to $6.7 \cdot 10^{10} \text{ W/m}^2$ in the working plane.

II.2. Material: Alloy 800H steel

Alloy 800H steel (also known as 1.4876) is an austenitic, heat-resistant iron-nickel-chromium alloy with controlled levels of carbon, aluminum, and titanium. This alloy is characterized by good creep rupture strength at temperatures higher than 600 $^{\circ}\text{C}$ and good resistance in oxidizing, nitriding, and carburizing conditions. A further advantage is its metallurgical stability in long-term

use at high temperatures. However, as mentioned above, the formation of “hot cracks” along fusion zone grain boundaries makes this alloy difficult to use even in conventional welding processes [16]. Sayiram and Arivazhagan [17] found that nickel-base filler materials can be used to minimize the risk of cracking in the arc welding process. Due to other technological principles, however, filler materials cannot be used in the LPBF process and, as a consequence, the use of A800H poses a challenge in terms of achieving defect-free parts.

In the present study, two types of materials were used. The chemical composition of both materials is shown in Table 1 (iron as a main element is usually not shown, n/d means no data available).

Table 1. Chemical composition of materials used.

Elements	C	S	Cr	Ni	Mn	Si	Ti	Cu	P	Al	Co	Mo
TLS, %	0.1	n/d	19.8	31.5	1.8	0.9	0.4	n/d	n/d	n/d	n/d	0.6
VDM, %	0.08	0.003	20.41	30.32	0.58	0.55	0.33	0.11	0.013	0.25	0.05	n/d

The first material used in the LPBF process was A800H powder with a particle size of around 50 μm . This powder was produced by TLS Technik GmbH & Co. SpezialPulver KG (Bitterfeld, Germany). The second material used was an industrial (rolled-sheet) plate with a thickness of 1 mm, which was provided by VDM Metals GmbH (Werdohl, Germany), and was used in Mössbauer studies. A very detailed characterization of A800H is given in the commercial material data sheet [18], including its physical-chemical, microstructural, mechanical, and other properties.

II.3. X-ray computed tomography

Micro-/nano-focus X-ray computer tomography (CT) is a non-resonant, non-destructive computerized X-ray method for studying multi-component materials and constructions in the 3D regime. It is currently the only method that allows the observation and analysis of the internal structures of sample objects, both organic and inorganic, with no sample preparation requirements (such as sectioning and grinding) and without strong limitations on the size and shape of the objects studied (i.e., compared with other high-resolution imaging techniques). CT can be used to detect the internal design of different components of a sample object – such as inclusions, distortions, inhomogeneity, and defects (porosity, cracks) – supported by a digital reconstruction of the 3D images and/or video obtained for the samples studied.

As part of several studies, X-ray CT measurements were carried out at ZEA-1 using recently upgraded industrial equipment (Fig. 2) and were tested in different fields. The performance of the CT setup installed at ZEA-1 was proved on the basis of examples from various scientific areas and applications. In particular, Natour and Pauly [19] demonstrated its wide range of applications through their analysis of organic materials to solid metal components such as welding and joining technologies. The implementation of new iterative reconstruction methods with a GPU-accelerated computer setup was considered by Götz et al [20] in order to improve the quality of CT images and optimize the computational costs for the CT setup at ZEA-1. The X-ray CT system shown in Fig. 2 was specifically designed in cooperation with the Development Center of X-ray Technology (EZRT, Saarbrücken, Germany) to meet the requirements of various fields of research, including materials for metallurgy, energy conversion, and storage. The system includes a high-precision setup on a granite base with air bearings, and features an enhanced geometric configurability within the 3D space with a reproducible accuracy of $< 1 \mu\text{m}$, as well as both micro- and nano-focus X-ray tubes, resulting in a resolution of up to 2–3 μm for appropriate contrast images. Various detectors of up to 4096² pixels and 40 cm² are available for different applications. As shown by the co-authors of this paper in previous studies, the actual X-ray CT configuration makes it possible to obtain 3D images of sample objects up to 50 cm in diameter in the real-time regime [17] and, as demonstrated by Pecanac et al [22], with a resolution of not less than $\sim 30 \mu\text{m}$ for ceramic materials. The XT9000-series nano- and micro-focus X-ray tubes are fabricated by Viscom AG (Hannover, Germany) and

their target material is tungsten [23]. The nano-focus X-ray tube has a finer focus spot size (about 900 nm), enabling higher-resolution 3D images to be obtained than with the micro-focus tube. However, the micro-focus tube has a higher radiation intensity, which is more suitable for obtaining the appropriate statistics for highly absorbing materials such as steel.

In this study, micro-CT studies were carried out for most samples in order to obtain a general overview. The typical parameter values for 3D image exposition were as follows: voltage of about 190 kV and current of about 250 μ A during a measurement time of approximately 1 hour. Nano-focus measurements were obtained for individual samples in order to observe detailed features of the internal structures. For these measurements, the typical parameter values for 3D image exposition were as follows: voltage of about 120 kV and current of about 80 μ A during a measurement time of approximately 3 hours. The voxel size for the samples investigated was varied around 15-30 μ m, typical filters used were copper plates with the thickness around 0.5 mm.



Fig. 2. X-ray CT setup at ZEA-1, Forschungszentrum Jülich GmbH. The left-hand gray section (A) is the mounting system for the micro-focus X-ray tube (exchangeable with the nano-focus X-ray tube), the middle section (B) is the mounting and motion system for the sample holder, and the right-hand blue-black section (C) is the detector system.

II.4. Conversion electron Mössbauer spectroscopy

Mössbauer spectroscopy (MS) is a highly sensitive method for the investigation of solid-state compounds, including iron-bearing compounds, as shown by Gütlich et al in their review work [24] on the basis of numerous investigations in different fields of material science. Klingelhöfer et al designed a portable backscattering Mössbauer spectrometer for ore detection on Mars and integrated it into the research equipment of NASA Mars rovers [25, 26]. These spectrometers were successfully tested for mineral exploration of commercial ore, as shown in comparison studies of bornite by Gainov et al [27] in particular. They were also used by Borgheresi et al to clarify the structural properties of bornite [28]. Furthermore, the Mössbauer effect has found applications in several fundamental areas, for example quantum computing, as proven by Vagizov et al [29]. The

main focus of MS is the identification of the phase composition of the materials under study according to their "fingerprint" (or etalon) Mössbauer spectra, as well as phase transitions, dependence on temperature and pressure, valence state of nuclei probes (i.e., Fe), crystal-chemical bonding, etc.

Conventional transmission MS is used to study bulk material, which is typically placed between the Doppler-modulated Mössbauer source and the detector. In this case, radiation passes from the source through the complete depth of the sample and directly to the detector. In the case of highly absorbing materials, for example iron, copper, tungsten, and other heavy metals, conventional Mössbauer radiation cannot penetrate dense materials.

Conversion electron Mössbauer spectroscopy (CEMS) is a relatively rare outgrowth of MS and, unlike transmission MS, is suitable for investigating the surface of complex highly absorbing samples. According to a theory developed by Salvat and Parellad [30], the radiation from the Mössbauer source interacts with the sample and leads to the emission of internal conversion electrons by the sample (from a depth of ca. 300 nm below the exterior surface of the sample). A conversion electron detector positioned on the same side as the source counts electron radiation and produces a CEMS spectrum.

CEMS on ^{57}Fe nuclei was used in this study to detect the iron-bearing phases (α steel, γ steel, Fe oxides, and others) at room temperature (RT) using a commercial WissEl Mössbauer spectrometer equipped with a standard ^{57}Co source (Ritverc, Russia); a more detailed description of the equipment is given in [31]. In order to fulfill the requirements of the CEMS detector to achieve optimal Mössbauer measurements, the samples were in the shape of disk plates, with a diameter of ca. 17 mm and thickness of ca. 1 mm. More details about the origin of the steel plates are given in Subsection III.3. A mathematical analysis of the experimental Mössbauer spectrum was carried out using the method of least squares under the assumption of Lorentz-shaped spectral lines. A metallic-iron foil at RT was used to calibrate the velocity of the Mossbauer spectrometer. Isomer shifts IS were referred to α Fe at RT.

II.5. Optical microscopy

In order to perform optical microscopy, the samples had to be cut from the LPBF parts. One cut was made perpendicular, and one parallel, to the build direction in the LPBF machine to see the difference in structure. For this purpose, a diamond wire saw was used to achieve a smooth surface. Subsequently, the samples were embedded in epoxy resin to prepare them for polishing. After grinding and polishing, the samples were investigated using a Polyvar MET optical bright-field microscope equipped with a Jenoptik ProgRes SpeedXT core 5 high-resolution digital camera.

II.6. Experimental procedure

All samples produced by means of LPBF technology were sorted into three groups. The first group of samples (eight "test" samples) was produced by means of LPBF and studied using a combination of CT and optics in order to find the optimal parameters for further manufacture of CAB prototypes. Due to the fact that there is less additive manufacturing experience with the rarely-used A800H steel, a wide LPBF parameter range was studied. This includes high laser beam deflection velocity up to 4000 mm/s and high powder layer thickness up to 360 μm . The focus was linear-like variation of energy per unit of volume E_V , which was calculated according to the following formula:

$$E_V = \frac{P_L}{v_L \times D_L \times (2 \times \omega_0 - \gamma_L)},$$

where:

E_V : energy per unit of volume,

P_L : laser beam power

v_L : laser beam deflection velocity
 D_L : powder layer thickness
 r_0 : laser beam radius
 y_L : overlap of the laser beam tracks

Because of the unpredictability of the A800H material behavior in LPBF process all test samples were manufactured and investigated in the step-by-step mode. After LPBF manufacturing of the first sample it was investigated by means of CT and optics to determine the internal structure in 3D regime. The knowledge of internal structure allows to define the parameter set for the manufacturing of second sample. This procedure allows to get the feedback into parameter optimization and it was repeated for all eight test samples. The results of this investigation are described in Subsection III.1. The preliminary conclusions devoted to optimization of LPBF parameter sets for manufacturing of CAB prototype are discussed in Subsection III.2. The second group is a special massive sample produced for the purposes of investigation with CT and CEMS with regard to two issues: appearance of hot cracks and potential changes in phase composition. This sample is discussed in Subsection III.3. The third group is the CAB prototype itself, which was produced based on the optimal parameters found from the previous two groups of samples. The properties of the CAB prototype after production, which were studied using CT and optics, are discussed in Subsection III.4.


III. RESULTS AND DISCUSSION





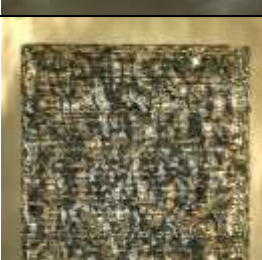
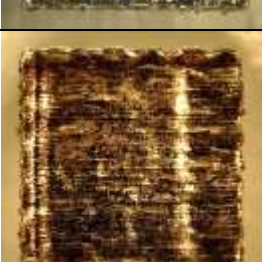

III.1. Test samples

For the test experiment, eight cubic test samples of $10*10*10 \text{ mm}^3$ were produced. Table 2 shows the LPBF parameters used as well as images of these samples. The main focus was the variation of energy per unit of volume (E_V) from low (No.1815) to higher (No.1823) values. Because of quite rare use of steel Alloy 800H in the LPBF process, the first order approximation could be based on the comparison with LPBF sets obtained for well-known and often used steel Alloy 316L. According to previous studies, for example Li et al. [32] and Cherry et al. [33], the decrease of energy per unit of volume E_V during LPBF manufacturing leads to a higher amount of pores. At the same time, steel 316L does not show other types of defects (e.g., hot cracks) [34].

As mentioned above, the manufacturing of samples and CT/optics investigation was made in step-by-step mode to get the feedback into parameter optimization. In order to obtain a linear-like variation of E_V , it was necessary to simultaneously adjust different LPBF parameters, for example laser beam power, velocity of laser beam deflection, overlap of laser tracks, and powder layer thickness. This is the reason for the large variety of values for the LPBF parameters shown in Table 2. After LPBF production, all samples were cut using a diamond wire saw and prepared for polishing (see Section II Materials and Methods).

Table 2. LPBF parameters for the production of 8 test samples.

Number	Laser power [W]	Velocity [mm/s]	Overlap [μm]	Layer thickness [μm]	E_V [J/mm^3]	Image $10*10*10 \text{ mm}^3$
032 1815	300	4000	30	45	50.5	

032 1816	62.5	500	10	45	52.4	
032 1818	50	150	0	45	117.6	
032 1819	100	350	10	45	119.8	
032 1820	50	150	5	45	127.7	
032 1821	100	150	10	90	139.8	
032 1822	200	150	15	180	154.3	
032 1823	350	150	25	360	170.6	

Remarks: beam profile: Gauss; beam diameter: 63 μm

From a general point of view, during the variation of LPBF parameters, we found a correlation between the LPBF parameters and the internal structure of the test samples, namely in terms of the character of defects that occurred (cf. Table 2). Changing the E_V value during LPBF manufacturing led to the occurrence of three types of typical defects: hot cracks, pores, and spatters. Spatters were observed in all samples and caused by evaporation of metal or humping form spherical particles during the melting process (this aspect is discussed below with more details in the context of sample No.1819). Pores dominated in samples produced with a low E_V value, whereas hot cracks were often found in samples produced with a high E_V value. The occurrence of three types of defects in case of steel Alloy 800H tells this alloy from the steel Alloy 316L, which demonstrates only one type - pores (see, for example, [32, 33]). We will therefore discuss three samples in more detail: No.1815 (Fig. 3), produced with a low E_V value; an intermediate case, No.1819 (Fig. 4), with a middle E_V value; and No.1823 (Fig. 5), with a high E_V value. All initial cubic samples after manufacturing were cut into two equal pieces: first one was used for CT investigation, whereas second one was for optical microscopy.

For sample No.1815, the minimal possible $E_V = 50.5 \text{ J/mm}^3$ was applied. The high laser beam velocity of $v_L = 4000 \text{ mm/s}$ led to minimal heat loss and, as a consequence, to an isotropic (3D), homogeneous, but defective sample structure with pores. The homogeneous distribution of defects confirmed the absence of large spatters and, as a result, uniform powder layers were obtained. Fig. 3a shows the corresponding optical microscopy (OM) image of the sample which was cut parallel to the build direction in the LPBF machine. This corresponds to the YZ cut in the nano-CT image shown in Fig. 3b. We found that the OM and nano-CT images are in agreement. Other images were obtained using only CT and are shown in Fig. 3c (XY cut) and Fig. 3d (XZ cut). The typical defect size does not exceed 0.35–0.4 mm across, while the pore size does not exceed 0.05–0.1 mm. As a note, the sample No.1815 was cut twice for two optical microscopy images. Therefore CT images (Fig. 3b,c,d) does not show the same shape of sample as CT images of other samples. In addition, the support structure was not removed after manufacturing and is observed as lines in Fig. 3b,c,d as well.

Sample No.1819 was produced with a higher E_V value = 119.8 J/mm^3 and a lower v_L value = 350 mm/s . The OM image shown in Fig. 4a demonstrates the appearance of narrow hot cracks ($< 0.02 \text{ mm}$ in width and $0.1\text{--}0.2 \text{ mm}$ in length) for the first time in contrast to the previous samples (Nos.1815–1818). As demonstrated by Nishimoto and Mori in their theoretical and experimental studies on steel [35], these hot cracks typically appear if the structure is overheated and experiences consequent high mechanical stress during cool-down. In addition, a large amount of defects caused by spatters ($0.3\text{--}0.5 \text{ mm}$ across) were found. Some small pores ($0.02\text{--}0.04 \text{ mm}$) and areas that were not completely melted ($0.8\text{--}1.5 \text{ mm}$ across) could be seen as well. Micro-CT confirmed the presence of defects caused by spatters and areas not completely melted (Fig. 4b,c,e). The occurrence of defects due to spatters has the following mechanism. During the melting process, the liquid metal spatters caused by evaporation of metal or humping form spherical particles. Some liquid metal spatters are welded to surface of the part under manufacturing due to its high temperature. This leads to the fact that the recoating blade of SLM machine cannot push it out of the laser scanning area. The size of these spatters is often many times higher than the powder layer thickness therefore the further powder coating is disturbed. Due to this fact, these defects have their own typical form and represent the spherical core (spatter) with several semi-round cavities or pore chains around. Fig. 4a demonstrates the optical image where these defects (spatters) can be clearly observed in red squared.

CT investigation detects all three types of defects (hot cracks, spatters and pores) as well (Fig. 4b,c,e,f) and in agreement with OM results. However, resolution of CT is not enough to distinguish the exact amount of these defects (especially in the case of small sizes, which are around and less than voxel size of CT) and to separate unambiguously all defects from each other, if these defects are located close to each other. Resolution in CT is actually limited not only by the measurement system, but also by the absorption and dimension of the sample. Because of the high

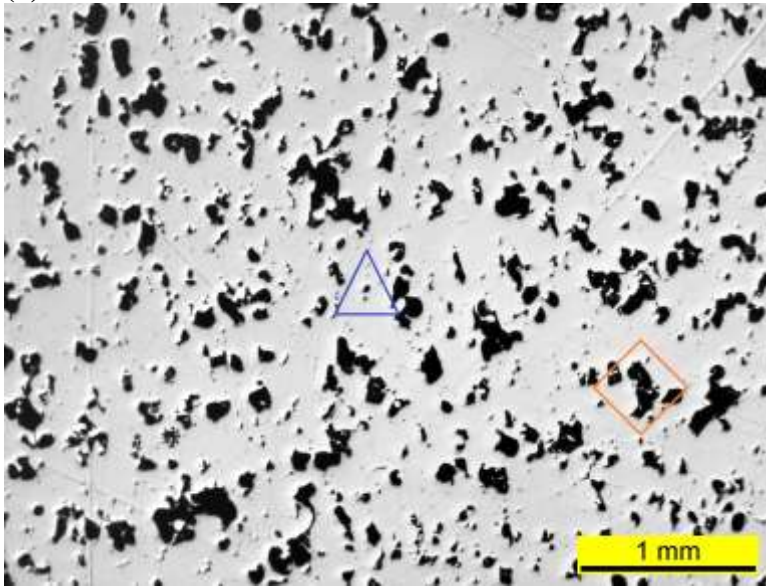
radiation absorption coefficients for metals (including steel), the reconstruction of defects is associated with measurement noise and artifacts. This effect may introduce a large error to determine porosity in the case of registering a small pore with a high surface area to volume ratio [36]. Similar situation can take place in the case of narrow hot cracks. Therefore, the combined use of CT and optical methods is highly encouraged approach. The use of optics, having better resolution, allows to check CT results in the case of indefinitely recognized defects and thus to be sure with conclusions. As it is shown in Fig. 4, optics does not reveal other types of defects regarding to CT.

On the other hand, the main advantage of CT is the ability to perform non-destructive investigations of the sample over the volume in 3D regime. The OM image (Fig. 4a) shows only one random 2D slice, whereas CT gives layer-by-layer information for all three projections. For example, Fig. 4b demonstrates the presence of a large amount of defects within the YZ projection at a given virtual position, whereas another virtual position of the YZ projection shows a substantially smaller number of defects (Fig. 4c). A similar situation exists for the XZ projection, as shown in Fig. 4e and Fig. 4f. This advantage offered by CT allows us to obtain a better understanding of the mechanism of defect building. One of the possible reasons for the large defects and areas not completely melted can be an inhomogeneous coating of steel powder within the layer. This inhomogeneity itself can be caused by defects within previous built layers.

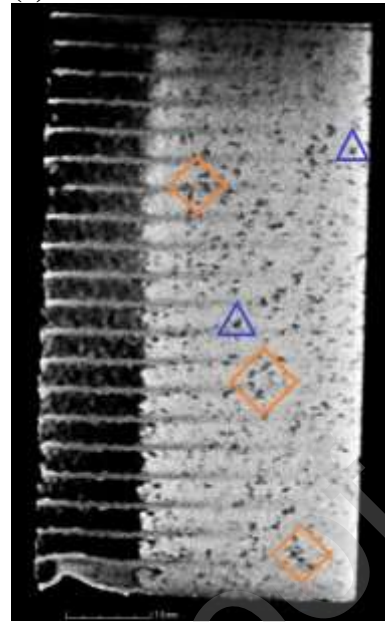
Sample No.1823 was produced with a higher E_V value =170.6 J/mm³. In order to reduce the negative influence of spatters on powder coating, the layer thickness was also increased to 360 μ m (in contrast to sample No.1819). Other parameters were adjusted to reach the desired E_V value. Both the nano-CT and OM methods found three types of defects: long hot cracks up to 1.2 mm in length, pores with a diameter up to 0.2 mm, and defects caused by spatters, with a size of around 0.5 mm across (Fig. 5). It is important to note that the nano-CT images show an absence of layer-by-layer distribution of defects in contrast to sample No.1819; in other words, the distribution of defects in each layer is more homogeneous.

The classification of pores could be preliminary done on the basis of investigation of eight test A800H steel samples (Table 2 and Figs.3-5) and its comparison with well-known 316L steel. Several reviews (see, for example, comprehensive work of Du Plessis et al. [11]) collect properties and reasons, obeying to keyhole mode porosity and lack-of-fusion porosity. As it is shown in the works of Gong et al. [37] and Tang et al. [38], keyhole porosity occurs when laser energy input (or energy density E_V) has too high value, whereas lack-of-fusion defects are observed at considerably lower laser energy input. Moreover, lack-of-fusion porosity decreases with increasing of E_V down to minimal value and keyhole porosity shows opposite dependence, i.e. this porosity increases with increasing of E_V . The behavior, corresponding to lack-of-fusion porosity, was observed by Li et al. [32] and Cherry et al. [33] during the studies of 316L steel. Separate investigation of 316L steel obtained by authors supports these data: in particular, the porosity is continuously decreasing with increasing of E_V from 23 to 58 J/mm³ at constant laser power of 156 W (internal results; published elsewhere in the future). This allows authors to suppose that the porosity in samples No.1815 and No.1816 (Table 2, Fig.3) manufactured at $E_V = 50.5-52.4$ J/mm³ can be attributed to lack-of-fusion type of defects, whereas sample No.1823 (Table 2, Fig.5) manufactured at much higher value $E_V = 170.6$ J/mm³ has keyhole mode porosity. In spite of the fact that the laser power in this work is varied as well (Table 2), the first order attribution could be reasonable. Nevertheless, this task requires further separate studies based on additional CT experiments (e.g., variation of LPBF parameters, leading to change of only one type of defect) and some theoretical principles due to the presence of three types of defects in A800H.

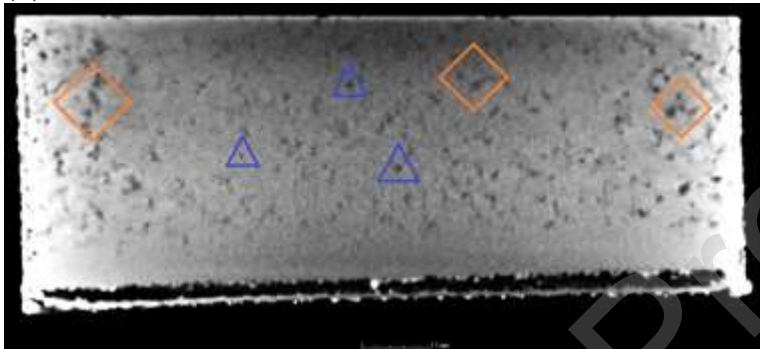
(a) OM YZ cut



(c) CT XY cut



(b) CT YZ cut



(d) CT XZ cut

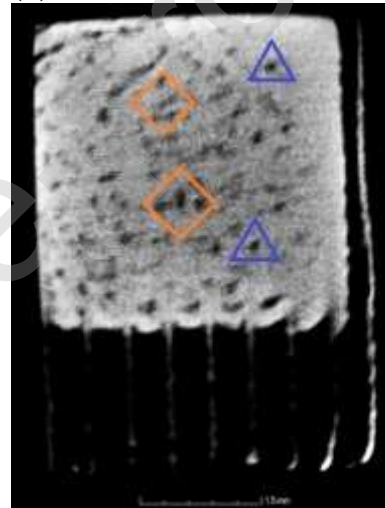
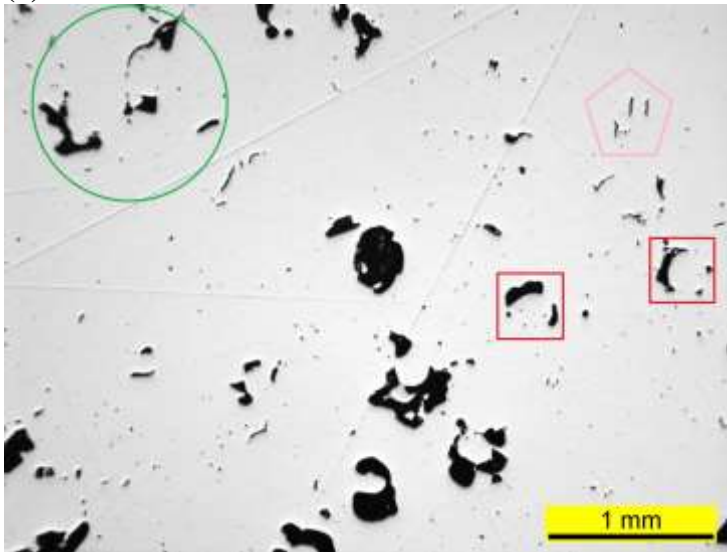
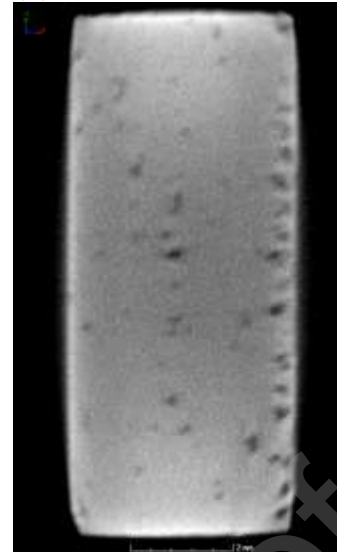


Fig. 3. Sample 1815: (a) Optical microscopy (OM) image in YZ projection; (b) nano-CT image in YZ projection; (c) micro-CT images in XY and (d) XZ projections. Blue triangles: pores; orange rhombs: defects due to pore clusters.

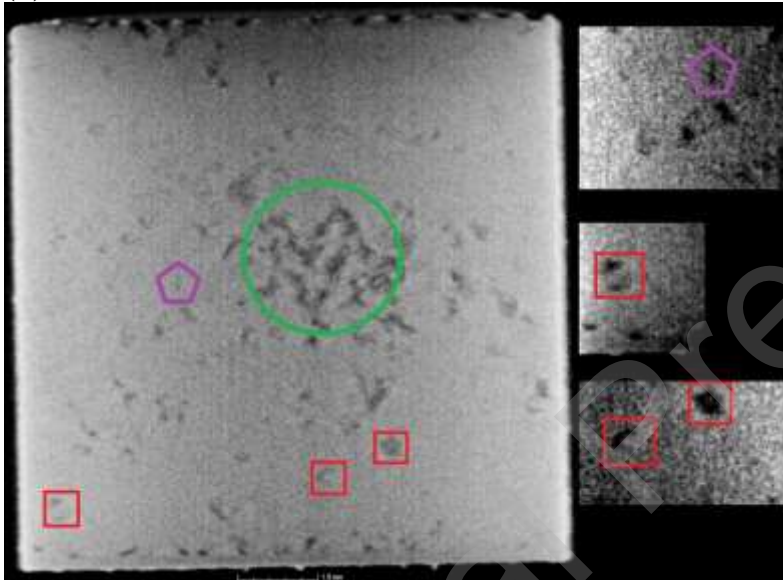
(a) OM YZ cut



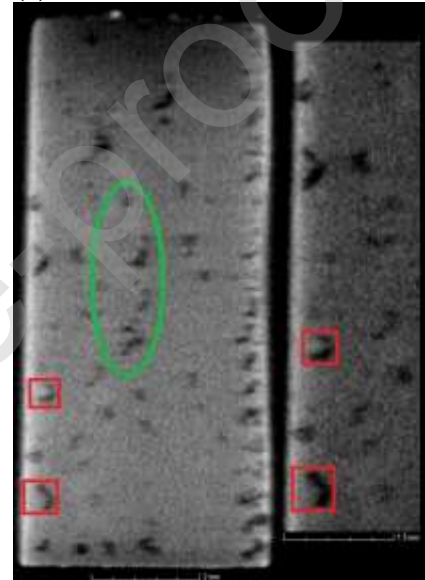
(d) CT XY cut



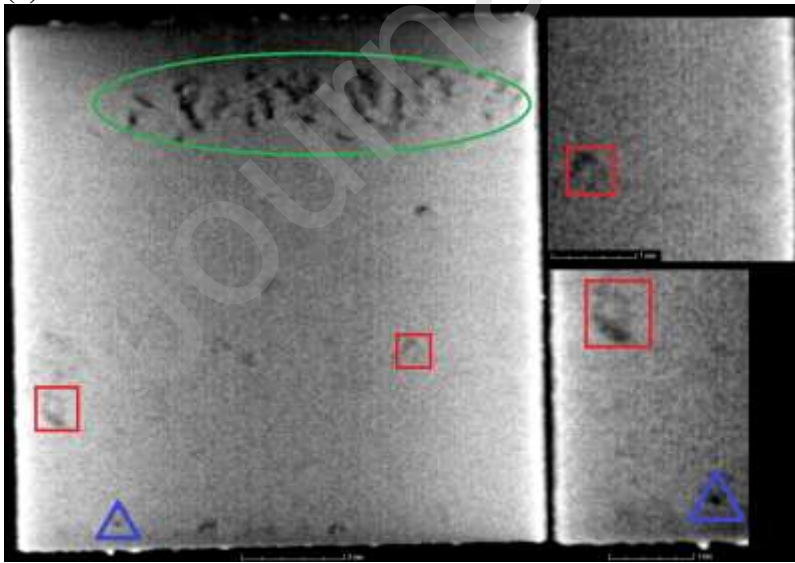
(b) CT YZ cut 1



(e) CT XZ cut 1



(c) CT YZ cut 2



(f) CT XZ cut 2

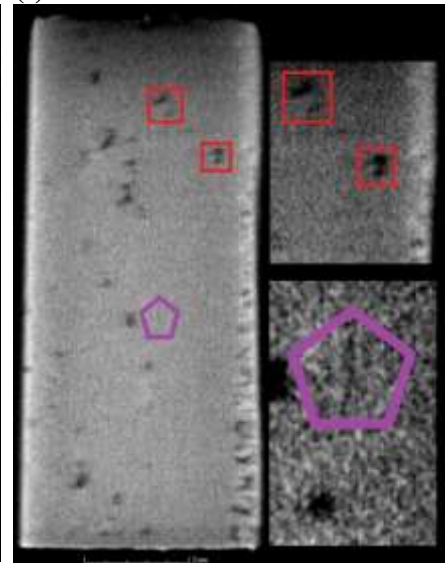
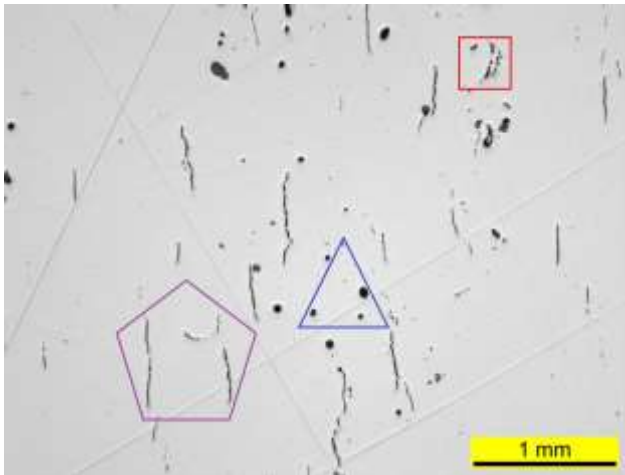
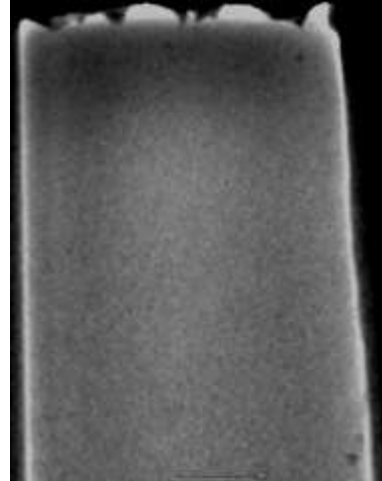


Fig. 4. Sample 1819: (a) Optical microscopy image in YZ projection, (b,c) micro-CT images in YZ, (d) XY (defects are not marked), and (e,f) XZ projections with the corresponding inserts, magnifying the views (various scales). Green circles: large unmelted areas; red squares: spatters; pink pentagons: hot cracks; blue triangular: pores.

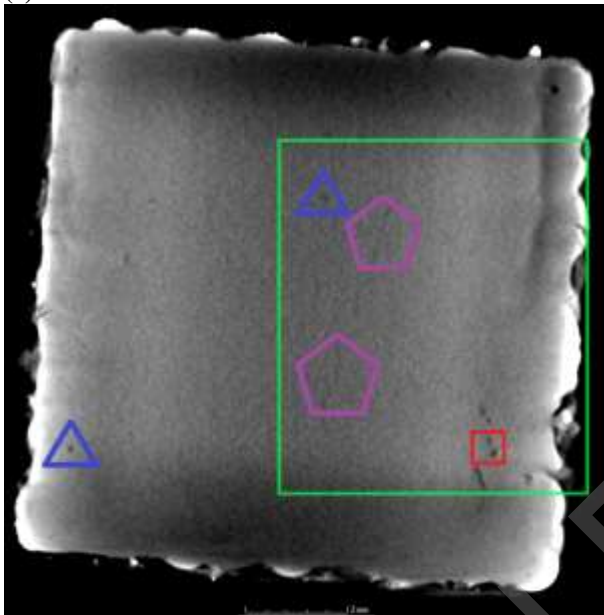
(a) OM YZ cut



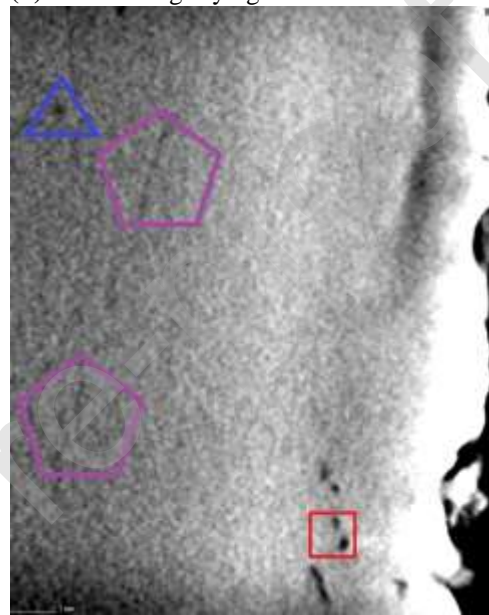
(b) CT XZ magnifying view



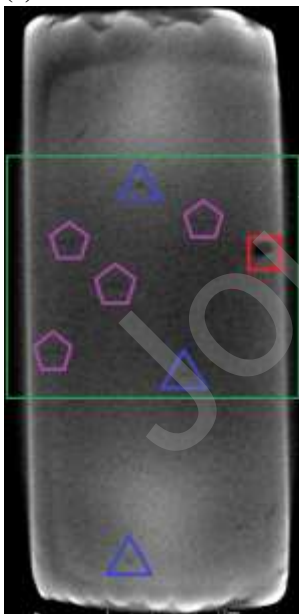
(c) CT YZ cut



(d) CT YZ magnifying view



(e) CT XY cut



(f) CT XY magnifying view

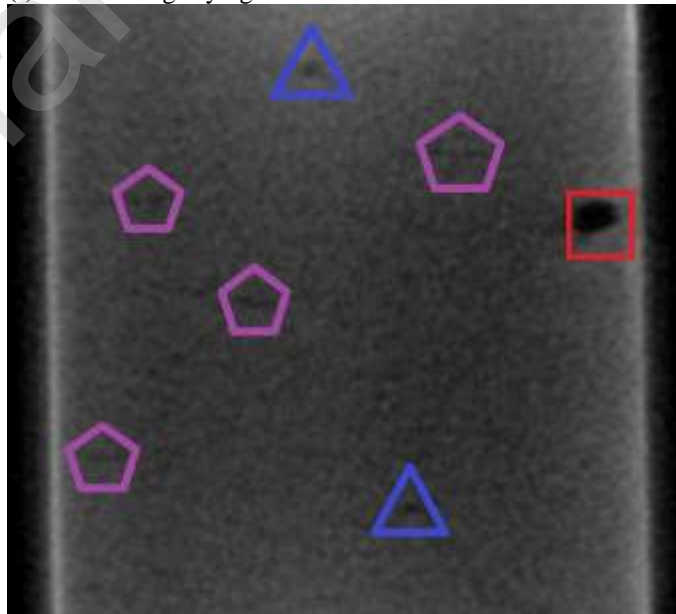


Fig. 5. Sample 1823: (a) Optical microscopy (OM) image in YZ projection, (b) nano-CT images in XZ (defects are not marked), (c,d) YZ, and (d,f) XY projections. Green rectangles show the areas, where the corresponding magnifying views on defects (various scales) are demonstrated by inserts on the right. Blue triangles: pores; red squares: spatters; pink pentagons: hot cracks.

III.2. Choice of the LPBF parameters for CAB prototype

As shown in Subsection II.6 and Subsection III.1, eight cubic samples ($10*10*10 \text{ mm}^3$) were manufactured by LPBF process from a rare used anti-corrodible high-temperature steel A800H in a wide LPBF parameter range. CT investigations in combination with optical microscopy in step-by-step mode made it possible to identify the defect types in the 3D regime and adjust the LPBF parameters accordingly. The final goal of this process was to find optimal parameter sets for the production of samples with minimal defect amounts and sizes. It was determined that in order to reduce the amount of pores, E_V should be increased. At the same time, in order to prevent hot cracks, E_V needs to be reduced. The balance value is about $E_V = 120 \text{ J/mm}^3$ for smaller bulk samples (thickness of around 10 mm). For thin steel parts, however, it is assumed that E_V should be less than 120 J/mm^3 in order to prevent overheating of the structure. The thin steel parts and components prevail in the case of CAB prototype for fuel cell device ([15] and Subsection III.4): the most internal walls and joining elements have the thickness in the range of 1-5 mm. This factor, as a consequence, let authors assume that the value of E_V can be considerably less than $100\text{-}120 \text{ J/mm}^3$ for the manufacturing of CAB prototype in order to decrease the overheating of thin elements and hot cracking. In practice, authors assigned a value of E_V for CAB as 88 J/mm^3 (Subsection III.4).

Another preliminary conclusion, which is important to optimize the LPBF parameter sets for manufacturing of CAB, concerns the decrease of spatter amount by two options. First, based on our investigation of all eight test samples (Subsection III.1), there is a tendency for decrease of spatters with decreasing deflection velocity of the laser beam. Second additional option to reduce the amount of spatters (sparks) is the use of the donut type laser beam profile [39]. Indeed, during the manufacturing of the test cubic samples using the Gaussian profile type made of the same steel A800H the unpredictably large number of spatters was observed in contrast to other types of steel (e.g., 316L). Based on the previous investigation [39, 40] the donut profile type demonstrates the same quality of performance like Gaussian profile type, but leads to the less number of spatters. As result, the donut type of laser beam profile was chosen for further manufacturing of special test "massive" sample (Subsection III.3) and CAB prototype itself (Subsection III.4).

The appearance of large amount of spatters in A800H steel parts could have two possible reasons. The sort of A800H steel should contain aluminum element in the range 0.15-0.30 %. This is in contrast to another sort of steel 316L, which does not have aluminum at all. During the welding process aluminum evaporates, leading to the expulsion of gases and melted metal. As a note, the manufacturer of A800H powder (TLS Technik GmbH, Subsection II.2 and Table 1), which is used in this work, does not provide information about exact aluminum content. Probably, this is caused by simplified method of chemical analysis for industrial products. Another additional reason is the 25 % lower heat conductivity of A800H steel (12 W/mk) regarding to 316L steel (15 W/mk). This circumstance could lead to the local overheating and expulsion of the material.

The motivation to manufacture the special test "massive" sample is caused by further optimization of LPBF parameters for CAB prototype and based on two reasons. First reason is demand to be sure that the performance in the case of donut type laser beam profile is not worse than the performance in the case of Gaussian profile. Second important reason is verification of phase composition of steel by Mössbauer spectroscopy. Next Subsection III.3 shows the results of Mössbauer spectroscopy investigation of test "massive" sample before the manufacturing of CAB prototype itself. Due to high sensitivity of Mössbauer spectroscopy to steel phase composition (austenite or magnetic steels) and corrosion (iron oxide family), the investigation of massive sample clarifies the following issue: do the extreme LPBF parameter sets for steel A800H avoid the appearance of parasite magnetic steel and corrosion centers. As it was found, even the extreme LPBF parameters (i.e., maximal laser power 275 W , leading to $E_V = 194 \text{ J/mm}^3$, Section III.3) do not influence on the A800H steel quality after manufacturing: there are no signatures of corrosion centers in the form of iron oxides and appearance of magnetic components of metal used. This result is very important due to the fact that the CAB prototype is intended for use together with a combination of the gases H_2 , CH_4 , and CO at high temperatures. This points out that the LPBF

parameters, which were used for further CAB manufacturing (e.g., less laser power 125 W, $E_V = 88 \text{ J/mm}^3$, Section III.4), do not expose to risk of corrosion or even magnetization. In this context these the LPBF parameter sets for CAB are assumed to be close to optimized parameters (Section III.4).

III.3. Massive sample and Mössbauer spectroscopy

The massive sample was produced as an additional test before the production of the CAB prototype itself. This sample represents an A800H steel cylinder measuring 110 mm in diameter and 32 mm in height (Fig. 6a). The manufacturing parameters were as follows: focused laser beam diameter: 100 μm (“donut” type); laser power: 275 W; $E_V = 194 \text{ J/mm}^3$; laser beam velocity: 450 $\text{mm}\cdot\text{s}^{-1}$; track-to-track overlap: $\approx 30 \mu\text{m}$; residual oxygen: $<0.1\%$. As mentioned in Subsection III.2, the donut type of laser beam profile was used to minimize the number of spatters for the massive sample and CAB prototype (Subsection III.4).

The main reason for producing this massive sample was to study the influence of high energy per unit volume (E_V) on the integrity of the massive metal sample. More specifically, the aim was to investigate defects when using a high E_V value (large-scale heating of massive construction) as well as possible oxidation and/or phase separation of the steel. It is possible that during the high-temperature LPBF manufacturing process, the austenite non-magnetic γ steel could undergo phase transition and transform partly and locally (within the massive sample) into a parasite, for example, magnetic α steel. Another topic of interest was the detection of potential traces of Fe oxides as a possible reason for crack enhancement.

As shown in Section II Material and Methods, from a technical point of view, CEMS can only study the surfaces of flat samples (of ca. 100–300 nm in depth for radiation penetration) with a diameter of 17–18 mm and a height of 1 mm. This was another reason to produce a preliminary massive sample. In order to study the interior of this sample, several cuts of 17 mm *1 mm were made at different depths.

In the study, three cut samples, referred to as CEMS plates, were obtained: "1O" which was cut 1 mm from the surface of the massive sample, "1M" cut 15 mm from the surface, and "1U" cut 30 mm from the surface. Similarly, cuts "2O", "2M", and "2U" were made at another part of the sample in order to check the results of the investigations for the first series of samples. Series 3 and 4 were retained as reserve CEMS plates in the event of uncertain CEMS results and were not investigated.

According to the micro- and nano-CT investigations of six CEMS plates (1O, 1M, 1U; 2O, 2M, 2U), all plates show the same type of structure. As an example, the YZ projection for sample 1M is shown in Fig. 6b. As expected, the structure shows a large amount of micro hot cracks due to the high E_V value (Fig. 6b, in red circles). The 5*5 mm^2 squares seen in the YZ projection (Fig. 6b, dashed blue square) are the results of the laser beam deflection strategy (“island” strategy). This island strategy helps to decrease the residual stress by melting the powder layers in a randomized checkerboard pattern. Along the borders of the squares, some defects due to the partly insufficient overlap of the “islands” are also observed (Fig. 6b, green rectangles). CEMS investigations of all six CEMS plates (sets 1 and 2) show the same results. Fig. 7 shows three CEMS spectra for LPBF samples 1O, 1M, 1U, one CEMS spectrum for an industrial VDM sample, and one separate MS spectrum.

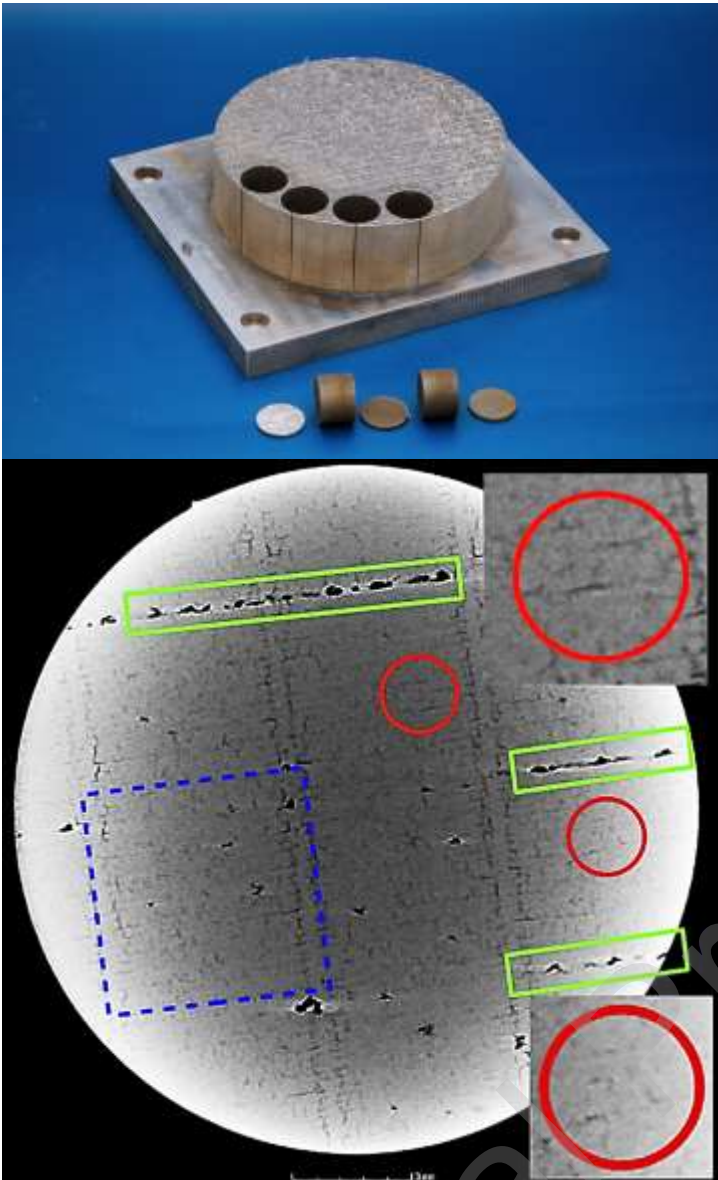


Fig. 6. Upward figure (a) is cylindrical massive sample on the substrate showing the 4 points at which cylinders for the CEMS plates were cut. Below the sample, CEMS plates 1O, 1M, and 1U are shown between the rest pieces; Downward figure (b) is micro-CT YZ projection of CEMS plate 1M (17 mm *1 mm): hot cracks are in red circles (also shown in corresponding insert loops); 5*5 mm² squares due to "island" strategy are in dashed blue square; defects due to the partly insufficient overlap of the "islands" are in green rectangles. See text for details.

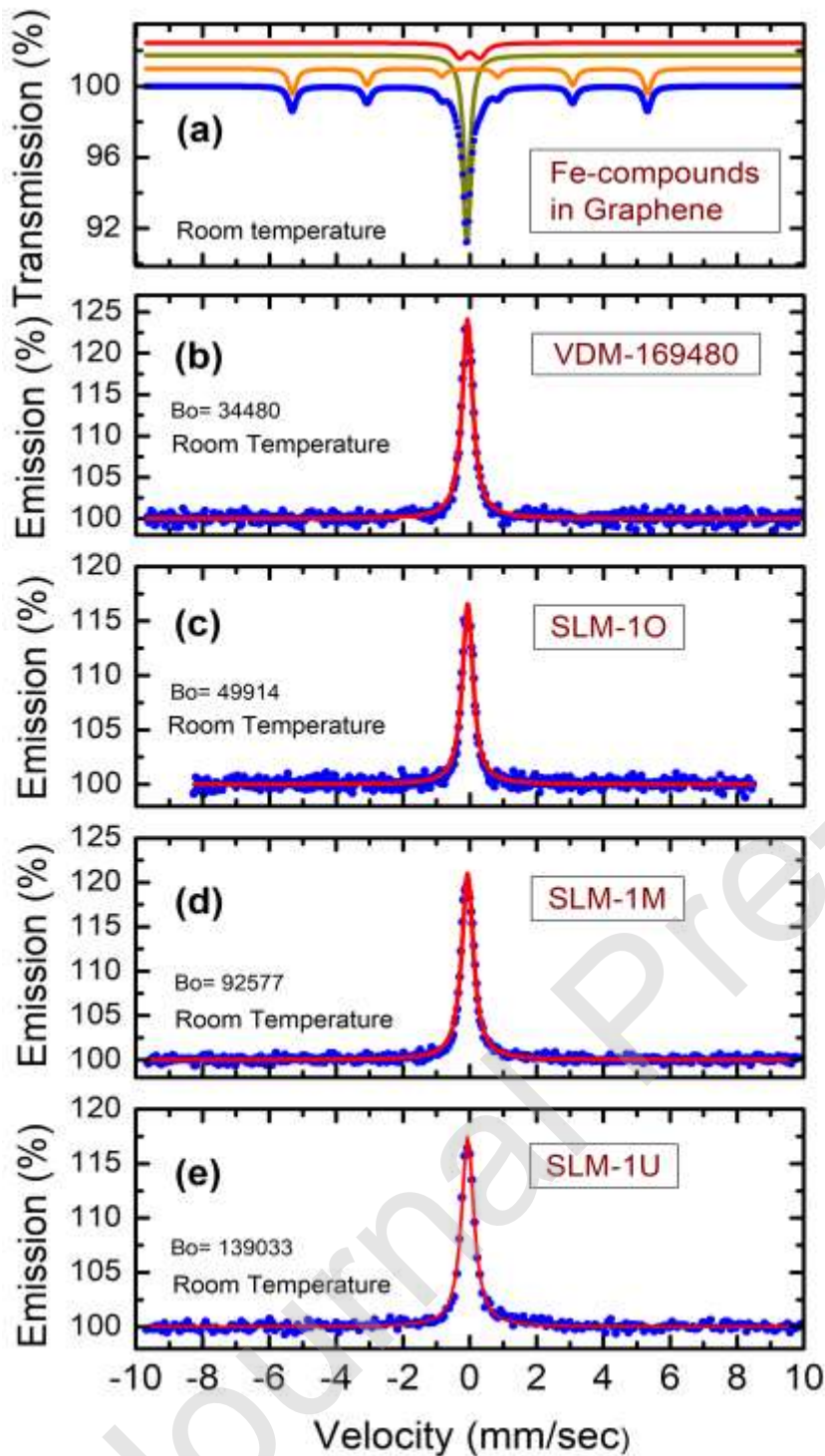


Fig 7. (a) Conventional ^{57}Fe -Mössbauer spectrum of separate sample, which contains a mixture of austenite non-magnetic steel (dark-yellow singlet), magnetic steel (orange sextet), and Fe-O oxide (red doublet) for comparison; (b) Conversion electron ^{57}Fe -Mössbauer spectrum of A800H steel industrial plate; (c,d,e) Conversion electron ^{57}Fe -Mössbauer spectra of LPBF-manufactured plates 10, 1M, and 1U. Blue circles represent experimental spectra for all images. Red singlet lines for (b,c,d,e) represent fitting curves.

This separate MS spectrum (Fig. 7a) was obtained by Khannanov et al [41] by means of transmission geometry (in contrast to CEMS) and demonstrates the formation of iron-based nanoparticles belonging to two iron allotropes with a body-centered cubic structure (α -Fe) and a face-centered cubic structure (γ -Fe) simultaneously. These iron-based nanoparticles were obtained on the graphene oxide support by means of thermal annealing.

As can be seen in Fig. 7(c,d,e), only one singlet line is observed in the case of LPBF samples with an isomer shift IS of between -0.06 and -0.08 mm/s, and a half-width HW varying between 0.38 and 0.44 mm/s. There are two main experimental facts. First, the CEMS spectra of the LPBF samples are nearly identical to the CEMS spectrum of the industrial VDM sample (roll-formed sheet, Fig. 7b), with $IS = -0.07(6)$ mm/s and $HW = 0.39$ mm/s. Second, in contrast to the iron-based nanoparticle sample (Fig. 7a), the CEMS spectra of the LPBF samples and the VDM sample do not contain any trace of sextet or doublet MS subspectra, typical for magnetic metallic iron (α -Fe) and magnetic iron oxides such as Fe_2O_3 , Fe_3O_4 , and paramagnetic FeO , within the experimental accuracy. This result points to an absence or, at least, a very negligible amount of such subspectra. As a consequence, the speculation that the steel quality will change and a corrosion effect will occur is ruled out by these investigations with overheating conditions in the LPBF-manufactured massive sample. In particular, the appearance of cracks in LPBF-manufactured samples is not affected by Fe-oxide compounds. This proves the anti-corrodible properties of LPBF-manufactured parts.

III.4. Cut made from CAB prototype

The design of the CAB prototype is complex and was previously simulated by Meißner et al [15]. The functionality of the CAB prototype is based on the original cone-like geometry with various thin walls, channels, and chambers (Fig. 8). The height of the cone-like CAB was 100 mm, the bottom diameter was 170 mm, and the top diameter was 90 mm. The most walls have the thickness in the range of 1 - 3 mm, joining elements rich around 5 mm.

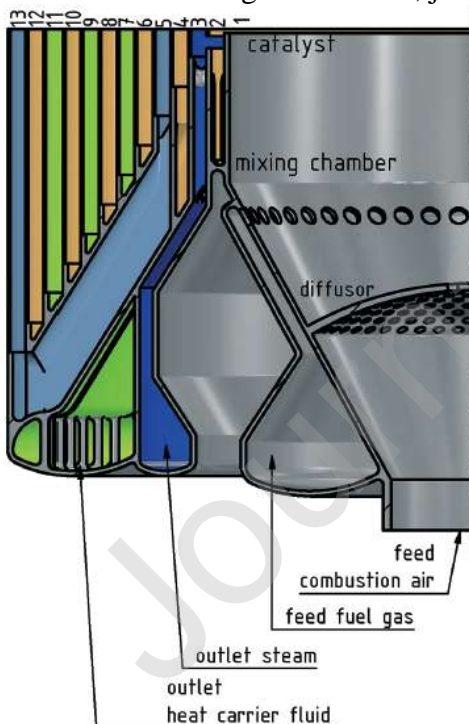


Fig. 8. Theoretical 3D model of a miniaturized cone-like CAB prototype for LPBF manufacturing, with the annotations indicating the functionality of the different channels, chambers, and other components. More details about the 3D model are given in a previous publication [11].

Based on previous experience in LPBF manufacturing of thin-wall structures and preliminary studies of eight test samples (Subsection III.1) and discussion of the choice for the manufacturing

(Subsection III.2), the CAB prototype was built using parameters with lower $E_v = 88 \text{ J/mm}^3$ in order to minimize the appearance of hot cracks. Other manufacturing parameters were as follows: focused laser beam diameter: $100 \mu\text{m}$ (“donut” type); laser power: 125 W ; laser beam velocity: $450 \text{ mm}\cdot\text{s}^{-1}$; track-to-track overlap: $\approx 30 \mu\text{m}$; residual oxygen: $<0.1\%$.

The CAB prototype was successfully built as shown in Fig. 9a. Later the entire CAB was mechanical cut on several pieces, having different dimensions, and two cut parts can be seen in Fig. 9b as example. The general structure of the CAB was approximately reproduced according to the 3D CAD model without explicit (visible) defects. All walls and channels were built with a smooth surface, as far as it can be judged from outside by the naked eye. As mentioned above, the entire CAB was mechanical cut on several pieces for further detailed measurements made by magnifying glasses, endoscopes and special straight rule. Authors compared the experimental dimensions and dimensions given in 3D-CAD model. The distinct distortions of the CAB construction and not-smooth surfaces were not found. Such an approach cannot be titled as all-embracing control, but this approach and cylindrical symmetry of CAB prototypes allows authors to assert that the CAB prototype is well reproduced.

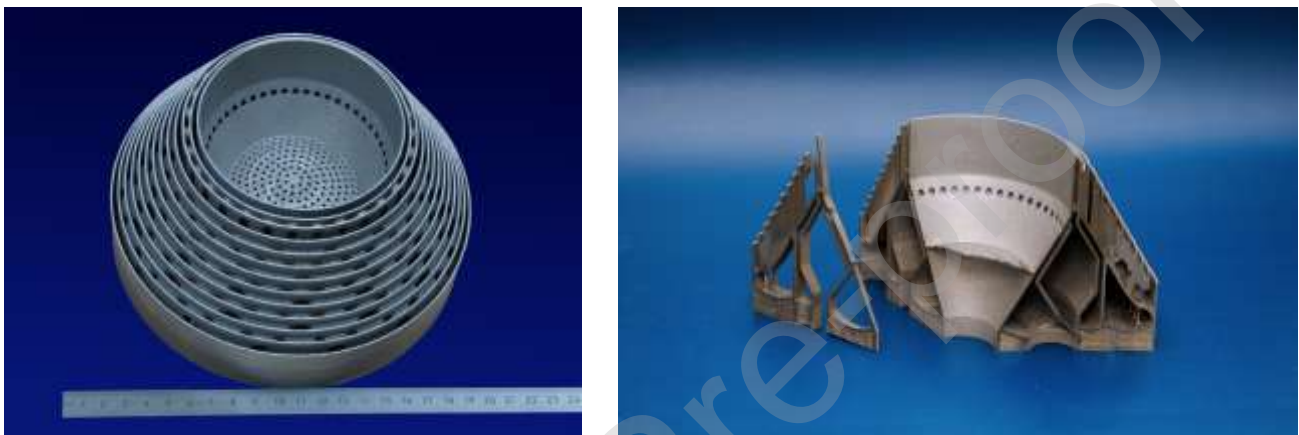


Fig. 9. (a) Cone-like CAB prototype after LPBF manufacturing; (b) two cut parts of the CAB prototype showing the complex internal design.

For a more detailed characterization of the structure, CT and optical microscopy were also applied. As noted above, the CAB prototype made of highly absorbing steel was large in size (90 mm in height and 170 mm in bottom diameter). This meant that it was not possible for X-ray radiation to penetrate the full CAB prototype or to perform high-quality 3D CT measurements. Several thin parts were therefore cut; one such typical part is shown in Fig. 9b on the left-hand side. The thickness of this part was about 10 mm at the outer diameter. Due to the high absorption of steel, only thin steel parts could be measured using CT (Fig. 10a and 10b).

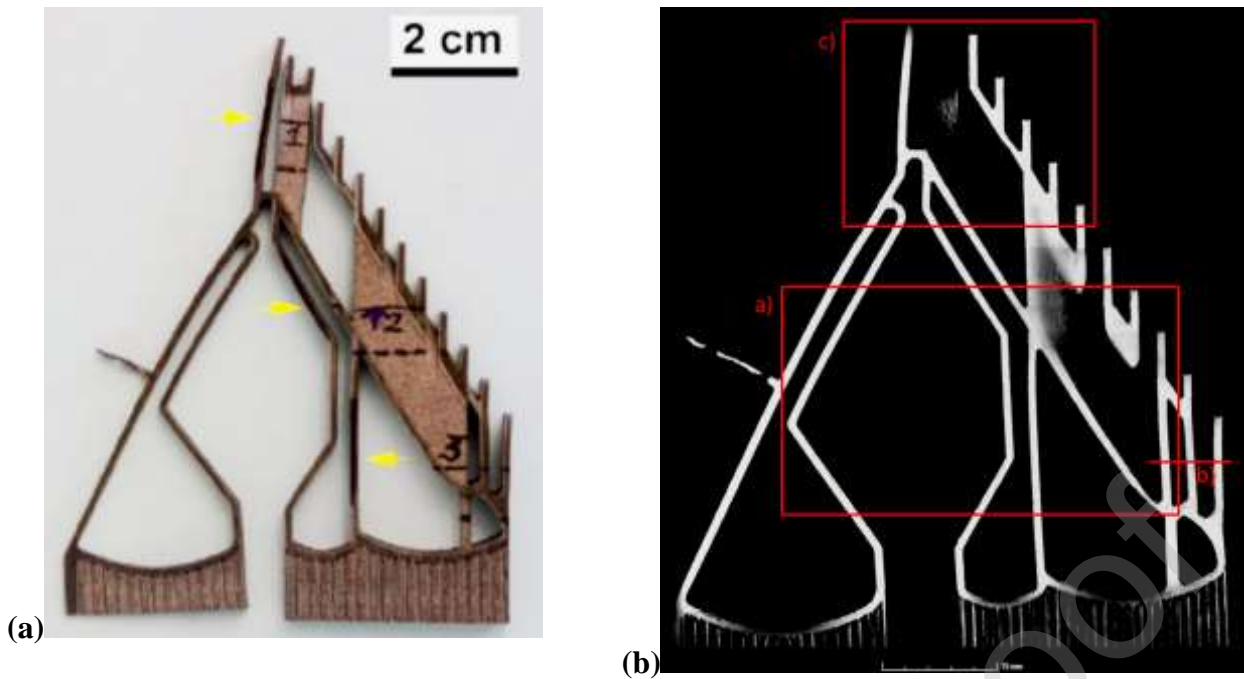
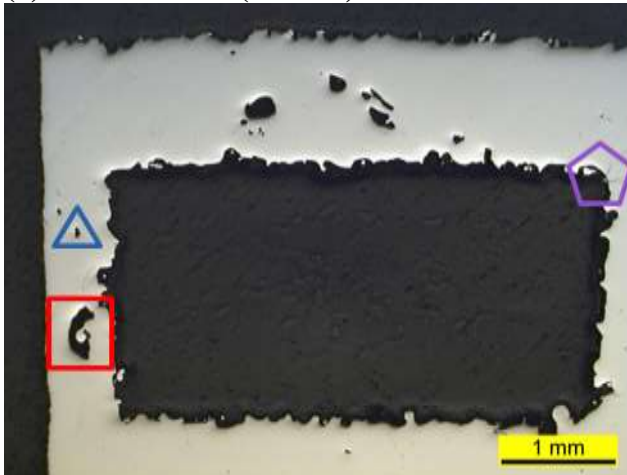


Fig. 10. CAB prototype: (a) Photo of the mechanical cut from the cone-like CAB prototype with three locations for optical measurements; (b) general 2D CT image of the mechanical cut from the cone-like CAB prototype with locations at which more detailed CT images with channel-like defects were taken (shown in greater detail in Fig. 12).

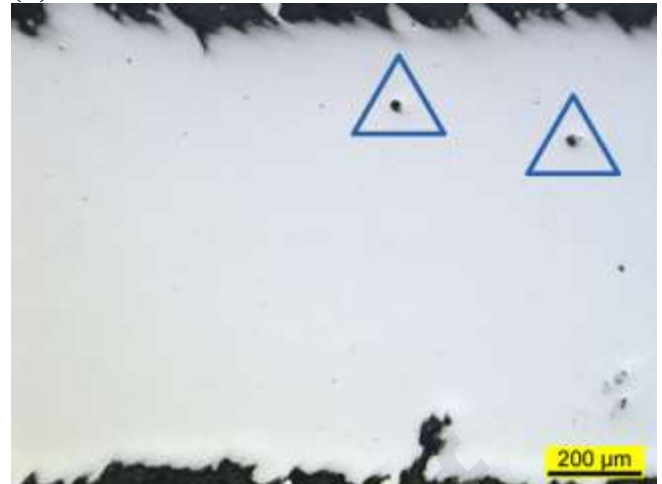
This thin steel part was subsequently also used to prepare the samples for optical microscopy. Three locations of cuts for optical measurements are shown in Fig. 10a. Fig. 11 shows the most representative optical microscopy images from all three locations. Analogously, the general CT view of the mechanical cut is shown in Fig. 10b, where three locations for further, more detailed CT analysis are also shown. These three more detailed CT images are presented in Fig. 12. In general, Fig. 11a shows that the structure of the part at position No.1 is built integrally, but has three types of defects that are typical for LPBF production: pores, hot cracks, and spatters.

The pores are rather infrequent distributed and have a typical size of 15–30 μm (Fig. 11b). According to experience of authors, such a distribution of pores should not significantly reduce the mechanical strength of the CAB construction. The hot cracks appear in the areas of the construction with a higher level of mechanical stress after LPBF manufacturing. For example, the sharp edges of the CAB construction initialize this type of hot cracks (Fig. 11c). Hot cracks also occur in the bulk of the walls due to overheating of the structure. The thickness of the hot cracks in the bulk is less than the thickness of the cracks around sharp edges. The spatters shown in Fig. 11a and Fig. 11d represent the most serious defects for the integrity of all thin constructions. This is due to the ratio of the thin walls (0.5–0.8 mm) to the size of the spatters (0.1–0.5 mm). It is important to note that the defects caused by spatters are not voids ("big" pores), but have bridges between the massive structure and the spatter itself. More detailed description of spatters is given in Subsection III.1. Because of this, the spatters could have an influence on the leakage of gases, but only have a slight influence on mechanical stability.

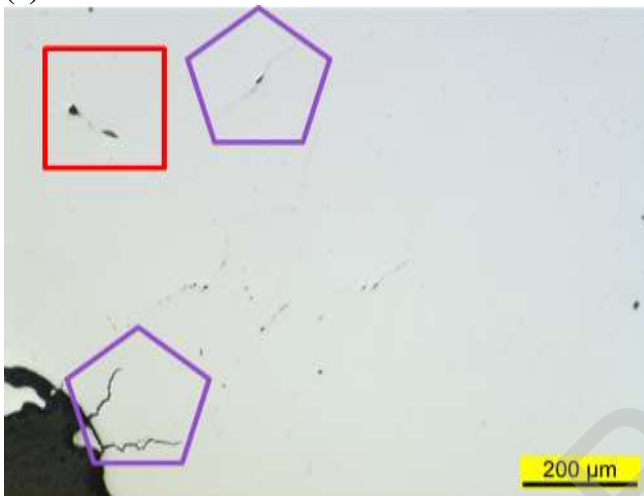
(a) General view (XY cut)



(b) XZ cut



(c) XY cut



(d) XZ cut



Fig. 11. CAB prototype: Optical microscopy images showing three types of defects: pores in blue triangles; spatters in red squares; hot cracks in violet pentagons.

Micro-CT confirmed the preliminary results of optical microscopy concerning the presence of defects (Fig. 10b), and also provided new information. In general, the walls seem to have an integral-like structure. The geometry of the CAB pieces, which were investigated by CT, was manufactured according to the basic 3D model and does not have large non-melted areas. However, the structure is not completely defect-free. Due to the virtual 3D option, micro-CT detected a new type of defect (Fig. 12a). These defects seem to be channel-like and located mostly in the middle of the walls (the wall thickness is 1 mm). These channel-like defects have an elliptic cross section with a semi-minor axis up to 0.3 mm and a semi-major axis up to 0.85 mm. Their lengths are variable and pass through several hundred LPBF powder layers (e.g., with the LPBF parameters used, there are 20 layers in 1 mm). The occurrence of the channel-like defects is not regular and seems to be rather sporadic. Although their origin is not entirely clear, it is possible to find a hypothesis. One potential explanation is the melting strategy of powder layers by the laser beam. Namely, the contour of the wall is melted first, and some powder from the core zone of the part layer is moved to the melting pool, resulting in the contour being built higher than the layer thickness (Fig. 12d). Only after melting is the core of the wall built by the laser beam, but it is built below the layer thickness (Fig. 12c, d). This leads to a lack of powder at the borderline between core and contour, with the result that the gap cannot be closed and a defect may occur (Fig. 12d). This mechanism is repeated for each layer and can thus lead to channel-like defects. Spatters may influence the enlargement of these defects.

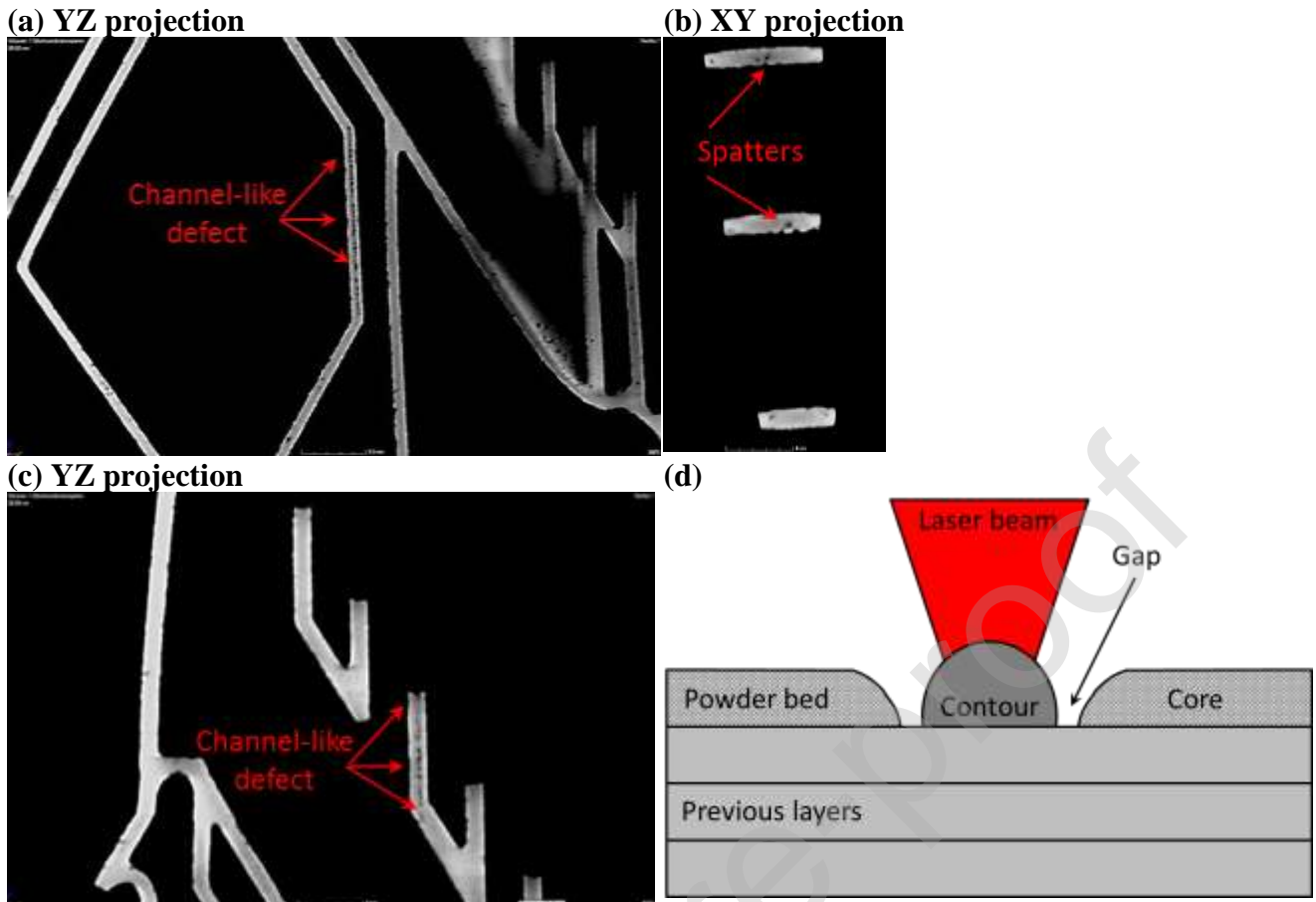


Fig. 12. Micro-CT images showing channel-like defects (a, c) and spatters (b) inside of CAB prototype; diagram showing the possible mechanism of appearance of channel-like defects (d).

Conclusions and outlook

The anti-corrodible high-temperature steel A800H is difficult to use even with conventional welding [16] and, as a consequence, its use poses a challenge in the LPBF process. Due to this fact the effects of LPBF parameter variation on preliminary test samples were investigated by nano-focus CT and Optical microscopy. Three types of defects were detected: pores, hot cracks, and spatters. The parameter variation helped to elucidate the internal structure for further LPBF process optimization and manufacturing of CAB (Subsection III.2). However, without further studies and fine adjustment of the LPBF parameters, it is difficult to prevent fully the occurrence of all defects.

In spite of its complex geometry, LPBF manufacturing of the first prototype of a miniaturized CAB for fuel-cell applications was successful and was performed according to the initial 3D CAD model (Subsection III.4). CT studies demonstrated the integral (all-in-one-piece) and stable structure of the CAB, i.e. without any large deformation or internal destruction. Nevertheless, the structure was not completely defect-free. Three types of defects (pores, hot cracks, and spatters) were detected in accordance with the results of the preliminary studies. In addition, vertical channel-like defects in the CAB prototype were also found and were located rather sporadically throughout the entire structure. It seems that pores and spatters could be further reduced through fine adjustment of the LPBF parameters. Hot cracks could be prevented through heating of the LPBF chamber. On the other hand, the channel-like defects are more serious due to the unclear reason for their appearance. One possible reason for this type of defect is the melting strategy applied during the LPBF process. To counter this, the number of these defects could be minimized by means of additional powder application after the contour structure is melted.

Conversion electron Mössbauer spectroscopy (CEMS) studies of a special test bulk sample manufactured with an extremely high E_V value proved that phase separation does not occur during

the LPBF process and that hot cracks are not caused by the oxidation of steel. From this point of view, the choice of Alloy 800H is verified and seems to offer perspectives for further LPBF manufacturing as a result of the lack of corrosion domains in the structure of metal parts. This is very important due to the fact that the CAB prototype is intended for use together with a combination of the gases H₂, CH₄, and CO at high temperatures.

Based on the results of this work, it is obvious that for metal parts with complex geometry (such as CABs), the LPBF parameters should have different values for structures with different thicknesses and shapes, especially for parts made of problematic types of steel such as Alloy 800H. As an outlook for the future development of the LPBF process, authors suggest two options at least:

First, LPBF machines should distinguish the thickness of the structures of the individual part and adjust the LPBF parameters in an automatic regime. In particular, finer areas must be built using parameters with a lower E_V , while for thicker areas the E_V should be increased. This is caused by the fact that the thicker structures can accumulate energy (heat). On the contrast, the finer structures do not have this opportunity, leading to overheating of the whole structures. However, the issue of adaptive scanning strategy, depending on varied energy density, represents the challenge as well. This is due to the obvious changes of thermal gradients and, as result, appearance of new features in the structure, especially in the vicinity of border between thick and fine parts of the structure.

Second possibility for improving the properties of parts with a complicated design (e.g., the CAB prototype) is to combine different types of steel during LPBF production ("composite" steel construction from, for example, A800H and A800HP steels). One such approach for using powders from different materials is shown by Clare and Kennedy [42].

The options of adaptive scanning strategy and composite steel construction should be preliminary studied and checked before use. Computed Tomography has an important role to solve this problem as well.

Turning back to hot cracking itself, it is important to note that this effect is not reported much in the prior publications and, as consequence, is not studied well up to date. The hot cracking, which is formed in case of A800H steel, makes conventional welding very difficult [16]. This work confirms earlier results concerning the hot cracking in this steel by example of LPBF process and points to the possibility to minimize this effect. The findings assume that A800H steel could serve as a "proof" material for further studies in order to understand this phenomenon. The hot cracking represents the complex effect and the complementary investigations are expected.

In conclusion, LPBF manufacturing of geometrically complex structures (e.g., a miniaturized CAB for fuel cells) from high-temperature anti-corrodible Alloy 800H steel has considerable potential, in spite of the fact that Alloy 800H is widely considered as an unpredictable and difficult type of steel for welding and additive manufacturing technologies. However, LPBF manufacturing using Alloy 800H requires further investigation to improve the quality of the parts. The example of the CAB prototype provided in this paper proves that LPBF offers good prospects for the production of key devices made of Alloy 800H in the field of conversion energy and storage, which are difficult and expensive to manufacture using traditional methods.

Author's statement:

Dr. Ramil Gainov:
Conceptualization;
Investigation;
Data Curation;
Writing - Original Draft, Reviewing and Editing

Dr. Dietrich Faidel

Methodology;
Investigation;
Writing- Reviewing and Editing

Dr. Wilfred Behr
Validation

Professor Ghaleb Natour:
Supervision

Dipl.-Ing. (DE) Fred Pauly
Investigation;
Validation

Dr. Holger Willms
Project administration

Professor Farit Vagizov
Investigation

Journal Pre-proof

Journal Pre-proof

Literature

- [1] Faidel, D., Jonas, D., Natour, G., Behr, W., 2015. Investigation of the selective laser melting process with molybdenum powder. *Additive Manufacturing* 8, 88-94. <https://doi.org/10.1016/j.addma.2015.09.002>
- [2] Bremer, S., Meiners, W., Diatlov, A., 2012. Selective Laser Melting, A manufacturing technology for the future? *Laser Technik Journal*, 9(2), 33-38. <https://doi.org/10.1002/latj.201290018>
- [3] Weber, A., 2017. Additive Manufacturing Takes Off in Aerospace Industry, The electronic version is accessed from 25.04.2017 at <http://www.assemblymag.com/articles/93176-additive-manufacturing-takes-off-in-aerospace-industry>
- [4] Klempert, O., 2015. Teilerfolge beim 3-D-Druck in der Serienproduktion. *VDI Nachrichten*, 31. The electronic version is accessed at: <http://www.vdi-nachrichten.com/Technik-Wirtschaft/Teilerfolge-3-D-Druck-in-Serienproduktion>
- [5] Everton, S.K., Hirsch, M., Stravroulakis, P., Leach, R.K., Clare, A.T., 2016. Review of in-situ process monitoring and in-situ metrology for metal additive manufacturing. *Materials and Design* 95, 431–445. <http://dx.doi.org/10.1016/j.matdes.2016.01.099>
- [6] Banhart, J., Borbély, A., Dzieciol, K., Garcia-Moreno, F., Manke, I., Kardjilov, N., Kaysser-Pyzalla, A.R., Strobl, M., Treimer, W., 2010. X-ray and neutron imaging – complementary techniques for materials science and engineering. *International Journal of Material Research* 101(9), 1069–1079. <https://doi.org/10.3139/146.110382>
- [7] Treimer, W., 2010. Radiography and tomography with polarized neutrons. *Journal of Magnetism and Magnetic Materials* 350, 188–198. <https://doi.org/10.1016/j.jmmm.2013.09.032>
- [8] Sales, M., Strobl, M., Shinohara, T., Tremsin, A., Kuhn, L.T., Lionheart, W.R.B., Desai, N.M., Dahl, A.B., Schmidt, S., 2018. Three Dimensional Polarimetric Neutron Tomography of Magnetic Fields. *Nature Sci. Rep.* 8, 2214 (1-6). <https://doi.org/10.1038/s41598-018-20461-7>
- [9] Gainov, R.R., Mezei, F., Füzi, J., Russina, M., 2019. Design concepts for a supermirror V-cavity based combined beam polarizer and compressor system for the upgraded neutron time-of-flight spectrometer NEAT. *Nucl. Instrum. Methods Phys. Res. A.* 930, 42-48. <https://doi.org/10.1016/j.nima.2019.03.046>
- [10] Thompson, A., Maskery, I., Leach, R.K., 2016. X-ray computed tomography for additive manufacturing: a review. *Meas. Sci. Technol.* 27, 072001 (17pp). <https://doi.org/10.1088/0957-0233/27/7/072001>
- [11] Du Plessis, A., Yadroitsev, I., Yadroitsava, I. and Le Roux, S.G., 2018. X-ray microcomputed tomography in additive manufacturing: a review of the current technology and applications. *3D Printing and Additive Manufacturing*, 5(3), pp.227-247.
- [12] Shah, P., Racasan, R., Bills, P., 2016. Comparison of different additive manufacturing methods using computed tomography. *Case Studies in Nondestructive Testing and Evaluation* 6, 69–78. <http://dx.doi.org/10.1016/j.csnadt.2016.05.008>

- [13] Krakhmalev, P., Fredriksson, G., Yadroitsava, I., Kazantseva, N., du Plessis, A., Yadroitsev, I. 2016. Deformation behavior and microstructure of Ti6Al4V manufactured by SLM. *Physics Procedia* 83, 778-788. <https://doi.org/10.1016/j.phpro.2016.08.080>
- [14] Wits, W.W., Carmignato, S., Zanini, F., Vaneker, T.H.J., 2016. Porosity testing methods for the quality assessment of selective laser melted parts. *CIRP Annals - Manufacturing Technology* 65, 201–204. <http://dx.doi.org/10.1016/j.cirp.2016.04.054>.
- [15] Meißner, J., Weiske, S., Faidel, D., Tschauder, A., Samsun, R.C., Pasel, J., Peters, R., Stolten, D., 2017. Highly integrated catalytic burner with laser-additive manufactured manifolds. *React. Chem. Eng.*, 2, 437-445. <https://doi.org/10.1039/c6re00223d>
- [16] Lippold, J.C., 1984. An Investigation of Weld Cracking in Alloy 800. *Welding Journal* 63, 91-104. https://app.aws.org/wj/supplement/WJ_1984_03_s91.pdf
- [17] Sayiram, G., Arivazhagan, N., 2015. Microstructural characterization of dissimilar welds between Incoloy 800H and 321 Austenitic Stainless Steel. *Materials Characterization*, 102, 180–188. <http://dx.doi.org/10.1016/j.matchar.2015.03.006>
- [18] VDM, 2018. The electronic version is accessed at: https://www.vdm-metals.com/fileadmin/user_upload/Downloads/Data_Sheets/Datenblatt_VDM_Alloy_800_H.pdf
- [19] Natour, G., Pauly, F., 2014. Analysis of materials and structures in Scientific applications using micro focus computed tomography. *Key Engineering Materials*, 613, 239-243. . <https://doi.org/10.4028/www.scientific.net/KEM.613.239>
- [20] Götz, G., Schramm, N., Vogelbruch, J., Suslov, S., Pauly, F., Natour, G., Waasen, S., 2017. Fast iterative reconstruction: a comparison of hardware-accelerated techniques. *Proceedings of 7th Conference on Industrial Computed Tomography*, Leuven, Belgium. The electronic version is accessed at: <http://www.ndt.net/?id=20825>
- [21] Pauly, F., Schröder, G., Patzak, R. 2007. Realtime-Röntgenbetrachtung von Schweißprozessen mit direkter Fehlerauswertung. *DGZfP-Berichtsband BB 104 – CD*, Fürth, Germany. The electronic version is accessed at: <https://www.dgzfp.de/Dienste/Publikationen?kategorie=Berichtsb%C3%A4nde>
- [22] Pećanac, G., Malzbender, J., Pauly, F., Fontaine, M.L., Niehoff, P., Baumann, S., Beck, T., Singheiser, L. 2015. Mechanical characterization of ceramics by means of a 3D defect analysis. *Ceramics International*, 41, 2, Part A, 2411–2417. <https://doi.org/10.1016/j.ceramint.2014.10.055>
- [23] Viscom, 2018. The electronic version is accessed at: www.viscom.com/europe/products/manual-x-rayct/x-ray-tubes-xt9000/
- [24] Gütlich P., Bill E., Trautwein A.X., 2011. *Mössbauer spectroscopy and transition metal chemistry: fundamentals and applications*, Springer-Verlag, Berlin-Heidelberg, 585 p.
- [25] Klingelhöfer, G., Bernhardt, B., Foh, J., Bonnes, U., Rodionov, D., de Souza, P.A., Schröder, Ch., Gellert, R., Kane, S., Gütlich, P., Kankeleit, E. 2003. The miniaturized Mössbauer spectrometer MIMOS II for extraterrestrial and outdoor terrestrial applications: A status report. *Hyperfine Interact.* 144-145, 371-379. https://doi.org/10.1007/978-94-010-0045-1_36

- [26] Klingelhöfer, G., 2004. Mössbauer In Situ Studies of the Surface of Mars. *Hyperfine Interactions*, 158, 1–4, 117–124. <https://doi.org/10.1007/s10751-005-9019-1>
- [27] Gainov, R.R., Vagizov, F.G., Golovanevskiy, V.A., Ksenofontov, V.A., Klingelhöfer, G., Klekovkina, V.V., Shumilova, T.G., Pen'kov, I.N., 2014. Application of ^{57}Fe Mössbauer spectroscopy as a tool for mining exploration of Bornite (Cu_5FeS_4) copper ore. *Hyperfine Interact* 226, 51–55. <https://doi.org/10.1007/s10751-013-0980-9>
- [28] Borgheresi, M., Di Benedetto, F., Romanelli, M., Reissner, M., Lottermoser, W., Gainov, R.R., Khassanov, R. R., Tippelt, G., Giaccherini, A., Sorace, L., Montegrossi, G., Wagner, R., Amthauer, A., 2018. Mössbauer study of bornite and chemical bonding in Fe-bearing sulphides. *Physics and Chemistry of Minerals* 45(3), 227–235. <https://doi.org/10.1007/s00269-017-0911-4>
- [29] Vagizov, F., Antonov, V., Radeonychev, Y.V., Shakhmuratov, R.N., Kocharovskaya, O., 2014. Coherent control of the waveforms of recoilless γ -ray photons. *Nature*, 508, 80–83. <https://doi.org/10.1038/nature13018>
- [30] Salvat, F., Parellad, J., 1984. Theory of conversion electron Mössbauer spectroscopy (CEMS), *Nucl. Instr. and Meth. Section B*, 1, 1, 70-84. [https://doi.org/10.1016/0168-583X\(84\)90481-6](https://doi.org/10.1016/0168-583X(84)90481-6)
- [31] Wissel, 2018. The electronic version is accessed at: http://www.wissel-gmbh.de/index.php?option=com_content&task=view&id=53&Itemid=80
- [32] R. Li, J. Liu, Y. Shi, M. Du, Z. Xie. 316L Stainless steel with gradient porosity fabricated by selective laser melting; *J. Mater Eng and Perform* 19 (2010) 666. <https://doi.org/10.1007/s11665-009-9535-2>
- [33] J.A. Cherry, H.M. Davies, S. Mehmood, N.P. Lavery, S.G.R. Brown, J. Sienz. Investigation into the effect of process parameters on microstructural and physical properties of 316L stainless steel parts by selective laser melting. *J. Int. J. Adv. Manuf. Technol.* 76 (2015) 869. <https://doi.org/10.1007/s00170-014-6297-2>
- [34] G. Ziolkowski, E. Chlebus, P. Szymczyk, J. Kurzac. Application of X-ray CT method for discontinuity and porosity detection in 316L stainless steel parts produced with selective laser melting. *Archiv Civil Mech. Engineering.* 14 (2014) 608-614. <https://doi.org/10.1016/j.acme.2014.02.003>
- [35] H. Gong, K. Rafi, H. Gu, T. Starr, B. Stucker, Analysis of defect generation in Ti–6Al–4V parts made using powder bed fusion additive manufacturing processes, *Addit. Manuf.* 1 (2014) 87–98, <https://dx.doi.org/10.1016/j.addma.2014.08.002>
- [36] Kerckhofs, G. Schrooten, Validation of X-ray microfocus computed tomography as an imaging tool for porous structures, *Review of Scientific Instruments* 79 (2008) 013711.
- [37] M. Tang, P. C. Pistorius, J.L. Beuth. Prediction of lack-of-fusion porosity for powder bed fusion. *Addit. Manuf.* 14 (2017) 39–48. <https://doi.org/10.1016/j.addma.2016.12.001>
- [38] Nishimoto, K., Mori, H., 2004. Hot cracking susceptibility in laser weld metal of high nitrogen stainless steels. *Sci. Technol. Adv. Mater.*, 5, 231-240. <https://doi.org/10.1016/j.stam.2003.10.006>

- [39] Laskin, A., Faidel, D., Laskin, B., 2018. Optics to control thermal effects in selective laser melting. Proc. SPIE, 10523, Laser 3D Manufacturing V, 1052319 (26 February 2018). <https://doi.org/10.1117/12.2289683>
- [40] Faidel, D., Laskin, A., Behr, W., Natour, G., 2016. Laser beam shaping in optical systems of the selective laser melting machines (in Russian with English abstract). Journal proceedings of the II International conference “Additive technologies: present day and the future”, St.Reg.El.Pub., 0321601267 (16 March 2016). <https://conf.viam.ru/conf/192/proceedings>
- [41] Khannanov, A., Kiiamov, A., Valimukhametova, A., Tayurskii, D.A., Börrnert, F., Kaiser, U., Eigler, S., Vagizov, F.G., Dimiev, A.M., 2018. Gamma-iron phase stabilized at room temperature by thermally processed graphene oxide. J. Am. Chem. Soc. 140, 9051–9055. <https://doi.org/10.1021/jacs.8b04829>
- [42] Clare, A.T., Kennedy, A., 2016. Additive Manufacturing. US-Patent US 2016/0279703 A1 <https://patentimages.storage.googleapis.com/03/41/cc/b5ce04d012d1ed/US20160279703A1.pdf>

Journal Pre-proof